



LES study of turbulent flow fields over a smooth 3-D hill and a smooth 2-D ridge



Zhenqing Liu^a, Takeshi Ishihara^b, Takahiro Tanaka^b, Xuhui He^c

^a School of Civil Engineering & Mechanics, Huazhong University of Science & Technology, Wuhan, Hubei, China

^b Department of Civil Engineering, School of Engineering, The University of Tokyo, Tokyo, Japan

^c School of Civil Engineering, Central South University, Changsha, Hunan, China

ARTICLE INFO

Article history:

Received 8 July 2015

Received in revised form

29 January 2016

Accepted 6 March 2016

Keywords:

3-D hill

2-D ridge

Large eddy simulation

Turbulent flow fields

Spectrum

ABSTRACT

Large eddy simulation is applied to study the turbulent flow fields over a 3-D hill and a 2-D ridge with smooth ground. The mean velocities as well as the turbulent fluctuations are computed. Fairly good agreements with experiments validate the accuracy of the numerical model applied in this study. The spectra of the velocities in the wake of the 3-D hill and 2-D ridge, and those over the flat terrain, are calculated. Spectra of velocity fluctuations at selected locations in the wake of topographic features are well reproduced. The examination of spectra shades some lights on the dynamics of the turbulent flow. It is found that the spectra of fluids in the wake are sensitive to the oncoming turbulence condition for the 2-D ridge, which is not true for the 3-D hill. Non-isotropic characteristics of turbulence in the near-wake of topographic features are examined using ratios of Reynolds stress which are also compared with those in IEC 61400-1 (2005).

© 2016 Elsevier Ltd. All rights reserved.

1. Introduction

Prediction of the turbulent flow fields over curved topography is important for many engineering applications, such as safety of structures, wind damage to agriculture, aviation safety. It also plays a critical role in mapping the wind energy over complex terrain. This is important, because wind energy production is proportional to the cubic of wind speed. The wind resource is rich in some mountainous regions, but the distribution of wind speed is very complex, therefore an accurately prediction of the wind speed and the turbulence statistics of the flow over curved topography is now becoming more and more important. In the case of flow over curved topography, the flow fields in the wake are very sensitive to the oncoming flow condition which affects the locations of the separation and reattachment points. It makes the study about this kind of wake flow difficult. Before carrying out the study of the flow over real complex terrain, it is reasonable to firstly consider some simplified topography, like a 3-D hill or a 2-D ridge. In the past decades intense researches about these two cases have been carried out experimentally and numerically.

Experimental wind tunnel measurements of airflow over a three-dimensional circular hill and a two-dimensional ridge were made by Gong and Ibbetson (1989). In that study the experimental results and various theoretical models of the flow were compared. It was concluded that all linear models fail in the wake region where the mixing-length closure is no longer appropriate and the flow is highly non-linear. The comparison between the measurement over

the two-dimensional ridge and the three-dimensional circular hill showed that the wakes of these two cases are very different. Ferreira et al. (1995) carried out an experimental study of the turbulent isothermal flow around two-dimensional sinusoidal hills whose results indicate that the extension of the recirculating region is strongly dependent on the hill shape. Ishihara et al. (1999) examined the turbulent flow over a three-dimensional circular hill using split-fiber probes designed for measuring flows with a high turbulence and separation. The measurements from split-fibers and those from X-wires were compared and showed discrepancies between them. The advantages of split-fibers are presented. Spectrum analysis in that study shed lights on the dynamics of the wake flow and a low-frequency motion of the flow in the wall layer was identified. Ishihara et al. (2001) then did another experimental study about the flow fields over a two-dimensional ridge and compared the results with those over a three-dimensional circular hill. Considerable differences between these two cases on the lee side were found. Opened streamlines are identified in the wake of the 3-D hill, while closed ones are found in the wake of the 2-D ridge. The reason of this different flow patterns was explained from the view of the continuity equation. Cao and Tamura (2006) experimentally studied the turbulent boundary layer flow over a 2-D steep hill. The effects from roughness were also examined. In that study it was found the fractional speed-up ratio on the crest depends on both the hill surface condition and the upstream surface condition. This dependence becomes stronger with approaching to the hill surface. However, the comparison about the Reynolds

stress ratios over complex terrain proposed in IEC 61400-1(2005), which is an International Standard published by the International Electrotechnical Commission regarding wind turbines Design requirements., is lacked.

With the advancement in the computer technology, many numerical studies have been conducted, see Ferreira et al. (1995), Sajjadi et al. (2001), Ishihara and Hibi (2002), Lun et al. (2003), Iizuka and Kondo (2004), Iizuka and Kondo (2006), Tamura et al. (2007), Wan and Porté-Agel (2011), Cao et al. (2012), and Diebold et al. (2013). Based on these works, two major approaches can be classified.

The first approach is based on the Reynolds averaged turbulence model. In the study by Ferreira et al. (1995), the turbulence was modeled with a modified low-Reynolds number k - ϵ model. The flow pattern in the wake was successfully reproduced but the over-estimation of the speedup ratio at the crest of hill was obvious. A standard k - ϵ turbulence closure and a finite element integration technique were applied to the separated flows over 2-D hills. The results for the hills with gentle slopes were overall better than those with steep slopes. It was also found that the results for the cases with rough ground agreed better with the experiment than those with smooth ground. This indicates an application scope of the k - ϵ turbulence model for the flows over curved topographies. Sajjadi et al. (2001) did a numerical study and developed a realizable Reynolds averaged turbulence model in order to allow extrapolation to more practical situations. They suggested using TCL (two component limit) model for predicting the turbulent stresses over complex terrains when the Reynolds number is low. But in the separation region, the TCL model still underestimates the level of Reynolds stresses. Ishihara and Hibi (2002) numerically investigated the turbulent wake flow behind a three-dimensional steep hill with rough ground using standard k - ϵ model and Shih's nonlinear model which are all turbulence closure of Reynolds averaged approaches. They found that Shih's nonlinear model is better than the standard k - ϵ model. Flow patterns were also examined to explain the difference in the cavity zone between 3-D and 2-D hills. Lun et al. (2003) examined the performance of three types of turbulence models, i.e. standard k - ϵ , Durbin model as well as Shin's model in predicting the flow over a cliff and a hill. In that study Shih's model was also found to be the best choice in the models considered. Bitsuamlak et al. (2004) carried out a CFD study solving the Reynolds time-averaged Navier–Stokes equations and the standard k - ϵ turbulence model was used. Ground roughness and geometry approximation effects were also investigated. Bitsuamlak et al. (2004) then reviewed the numerical evaluation of wind flow over different types of topographies. They found that numerical simulations differing from one another by the type of numerical formulation followed, the turbulence model used, the type of boundary conditions applied, the type of grids adopted, and the type of terrain considered are summarized. Blocken et al. (2015) evaluated the accuracy of 3D steady Reynolds-averaged Navier–Stokes (RANS) simulations with a revised k - ϵ model for calculating mean wind-velocity patterns over this type of natural complex terrain. However, Reynolds averaged turbulence model can not provide the instantaneous flow fields, as a result there is no way to do the examinations for the dynamics of the flows which is also an important issue.

The second approach is based on the large eddy simulation. Iizuka and Kondo (2004) examined four sub-grid scale models for the prediction of flows over two-dimensional ridge. It was found that the results from the dynamic SGS models were in very poor agreement with those of experiment, whereas a hybrid SGS model, which is a combination of the standard Smagorinsky model and the dynamic Smagorinsky model, provides very accurate predictions. Iizuka and Kondo (2006) then studied the performance of another three modified SGS models and the best one (10 in their study, which models the SGS Reynolds stress by the scale-similarity concept) was

proposed. Tamura et al. (2007) carried out LES analyses to examine flow fields over 2-D hill models with steep and moderate slopes. The performance of two SGS models are studied and it was found that for the gently-sloping hill, both DSM (dynamic Smagorinsky model) and DMM (dynamic mixed model) results show sufficiently good agreement with experimental data. However, for a steep hill there is a clear discrepancy between LES and experimental turbulence statistics in the separated region. Tamura et al. (2007) then studied the turbulent boundary layer over a 3-D steep hill by large eddy simulation, in which DSM model was applied and the results showed sufficiently good agreement with experiments. The discrepancies between prediction and experiment were much smaller than those for 2-D ridge. Wan and Porté-Agel. (2011) used large eddy simulations to simulate stably-stratified turbulent boundary-layer flow over a steep two-dimensional hill. Three SGS models, i.e., Smagorinsky model, Lagrangian dynamic model and scale-dependent Lagrangian dynamic model, are examined. Among them the scale-dependent Lagrangian dynamic model lead to turbulence statistics more realistic than those obtained from the other two models. Cao et al. (2012) applied dynamic Smagorinsky model to numerically study the turbulent boundary layers over two-dimensional hills. The effects of roughness as well as the slope were also examined. The numerical results showed that when inflow turbulence and roughness are well modeled, reasonably good results could be achieved. Diebold et al. (2013) simulated the wind fields around a 3-D hill by large eddy simulations. Some inaccuracies near the ground and on the lee side of the hill were found and these were argued to be likely due to the fact that the separation point is hard to be resolved on a smooth surface. Abdi and Bitsuamlak (2014) examined the turbulence structure behind hills is using several turbulence models such as the mixing-length, standard k - ϵ , RNG k - ϵ , realizable k - ϵ and Smagorinsky LES models. They found that all turbulence models predicted Fractional Speed Up Ratio (FSUR) values on upstream side of hills adequately; but, the performance of simple turbulence models, such as mixing length, is found to be insufficient for characterizing wakes behind hills. However, the comparison of the spectrum of wind fluctuations in the wake of isolated hills between LES results and experimental data is limited.

In the present study, the standard Smagorinsky-Lilly model is applied and the flow fields over a 3-D hill and a 2-D ridge with smooth surface are examined. The details of the model including the numerical methods and the configurations of the numerical wind tunnel are introduced. Turbulent flow fields including the mean velocity profiles, turbulent fluctuations and the spectrum are presented. The Reynolds stress ratios are also examined and compared with those in IEC 61400-1 (2005).

2. Numerical model and boundary condition

The governing equations and the method simulating the roughness blocks are introduced in Section 2.1 and Section 2.2. From Section 2.3 to section 2.7 the configurations of the numerical wind tunnel, the mesh system, the boundary conditions, as well as the solution schemes, are presented.

2.1. Governing equations

Momentum and mass are primarily transported by large eddies; therefore, large-eddy simulation (LES) is adopted. In such simulations, large eddies are directly computed, while the influence of eddies smaller than grid spacing are parameterized. The Boussinesq hypothesis is employed, and the standard Smagorinsky-Lilly model (Smagorinsky, 1963) is used to calculate the subgrid-scale (SGS) stresses.

The governing equations are obtained by filtering the time-dependent Navier–Stokes equations in Cartesian coordinates (x, y, z) (Ferziger and Peric, 2002), which can be expressed as follows:

$$\frac{\partial \rho \tilde{u}_i}{\partial x_i} = 0 \quad (1)$$

$$\rho \frac{\partial \tilde{u}_i}{\partial t} + \rho \frac{\partial \tilde{u}_i \tilde{u}_j}{\partial x_j} = \frac{\partial}{\partial x_j} \left(\mu \frac{\partial \tilde{u}_i}{\partial x_j} \right) - \frac{\partial \tilde{p}}{\partial x_i} - \frac{\partial \tau_{ij}}{\partial x_j} \quad (2)$$

where \tilde{u}_i and \tilde{p} are the filtered velocities and pressure, respectively, μ is the viscosity, ρ is the density, τ_{ij} is the SGS stress, which is modeled as follows:

$$\tau_{ij} = -2\mu_t \tilde{S}_{ij} + \frac{1}{3} \tau_{kk} \delta_{ij}; \quad \tilde{S}_{ij} = \frac{1}{2} \left(\frac{\partial \tilde{u}_i}{\partial x_j} + \frac{\partial \tilde{u}_j}{\partial x_i} \right) \quad (3)$$

where μ_t denotes the SGS turbulent viscosity, \tilde{S}_{ij} is the rate-of-strain tensor for the resolved scale, and δ_{ij} is the Kronecker delta. The Smagorinsky–Lilly model is used for the SGS turbulent viscosity:

$$\mu_t = \rho L_s^2 |\tilde{S}| = \rho L_s \sqrt{2\tilde{S}_{ij}\tilde{S}_{ij}}; \quad L_s = \min(\kappa d, C_s V^{1/3}) \quad (4)$$

in which L_s denotes the mixing length for subgrid-scales, κ is the von Kármán constant, i.e., 0.42, d is the distance to the closest wall and V is the volume of a computational cell. In this study, C_s is Smagorinsky constant, which is set to be 0.1 for the atmospheric boundary layer (ABL) flow same as the study by Iizuka and Kondo (2006).

When the wall-adjacent cells are in the laminar sublayer, the wall shear stresses are obtained from the laminar stress–strain relationship:

$$\frac{\tilde{u}}{u_\tau} = \frac{\rho u_\tau y}{\mu} \quad (5)$$

If the mesh cannot resolve the laminar sublayer, it is assumed that the centroid of the wall-adjacent cells falls within the logarithmic region of the boundary layer, and the law-of-the-wall is employed as follows:

$$\frac{\tilde{u}}{u_\tau} = \frac{1}{\kappa} \ln E \left(\frac{\rho u_\tau y}{\mu} \right) \quad (6)$$

where y is the distance between the center of the cell and the wall, u_τ is the friction velocity, and the constant E is 9.793. In most of the region, the wall-adjacent cells are in the laminar sublayer.

2.2. Method simulating roughness block

Yamaguchi et al. (2009) have applied a method to simulate the canopy by adding an appropriate source term, $f_{\tilde{u},i}$, in momentum equation:

$$\rho \frac{\partial \tilde{u}_i}{\partial t} + \rho \frac{\partial \tilde{u}_i \tilde{u}_j}{\partial x_j} = \frac{\partial}{\partial x_j} \left(\mu \frac{\partial \tilde{u}_i}{\partial x_j} \right) - \frac{\partial \tilde{p}}{\partial x_i} - \frac{\partial \tau_{ij}}{\partial x_j} + f_{\tilde{u},i} \quad (7)$$

$$f_{\tilde{u},i} = -\frac{1}{2} \rho C_f \gamma_0 \tilde{u}_{mag} \tilde{u}_i \quad (8)$$

where $C_f = C_{D,\tilde{u}_i} / (1 - \gamma_0^2)$, C_{D,\tilde{u}_i} is the drag coefficient and determined as 0.4 following the suggestion from the study by Kaimal and Finnigan (1994). $\gamma_0 = V_0 / V_{grid}$ is the volume occupancy rate; V_0 is the volume occupied by the obstacle, and V_{grid} is the volume of the grid containing the obstacle; $l_0 = V_0 / A_0$ is the representative length; A_0 is the frontal area of the single roughness block.

Through the way modeling the roughness blocks introduced above, it is not necessary to explicitly build the geometry of the blocks. The volumes occupied by the roughness blocks could be determined by some functions. If the grid cells locate in the volumes, the drag force terms given in Eq. (8) will be added in the momentum equation to represent the effects of the solid blocks. If the arrangement of the roughness blocks is changed, it is not

necessary to rebuild the model. What we need to do is only to modify the functions determining the geometries of the blocks, avoiding the repeated works.

For the grids in the solid roughness blocks, $V_0 = V_{grid}$, therefore, volume occupancy rate γ_0 for the grids in the solid roughness blocks is 1.0, as a result, $C_d = C_f \gamma_0 / l_0$ is infinite. In this way, the velocities in the volume of the solid roughness blocks will be nearly zero. Therefore, the solid drag effects to the fluid could be reproduced.

2.3. Configuration of the numerical wind tunnel

In order to evaluate the performance of the numerical wind tunnel, data obtained from an experimental study by Ishihara and Hibi (1998) is used. The experiment was conducted in a return wind tunnel with a test section of 1.1 m wide, 0.9 m high and 7 m long. The neutrally stratified atmospheric boundary layer was simulated using 60 mm high cubic elements followed by 20 mm and 10 mm cubic blocks covering 1.2 m of the test-section floor. The areal densities of the roughness blocks with different sizes are same as those in the experiment, i.e., 25% for the blocks with height of 60 mm, 2.8% for 20 mm, and 0.7% for 10 mm. Each group of the blocks has three rows and the roughness blocks cover a region with length of 0.4 m in streamwise direction. The configuration of the numerical wind tunnel is same as that in experiment except the width of the wind tunnel and the upstream buffer zone, see Fig. 1, where the origin point is 3.4 m downstream of the roughness blocks. Fig. 2 shows the arrangement of the roughness blocks.

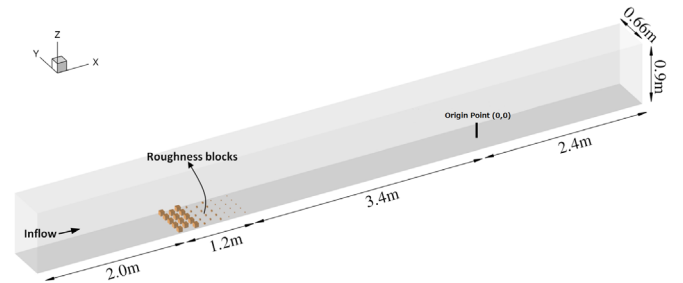


Fig. 1. Geometry of the numerical wind tunnel.

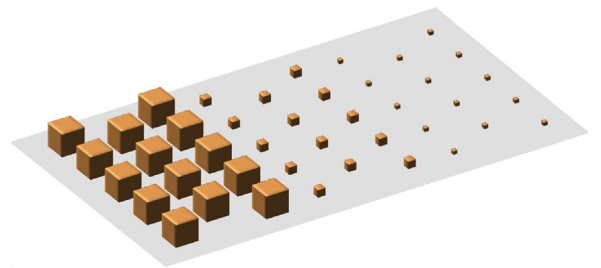


Fig. 2. Details of the arrangement of the roughness blocks.

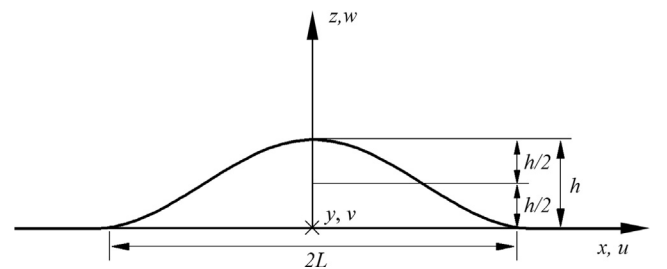


Fig. 3. Coordinates and notations of the 3-D hill and 2-D ridge used in this study.

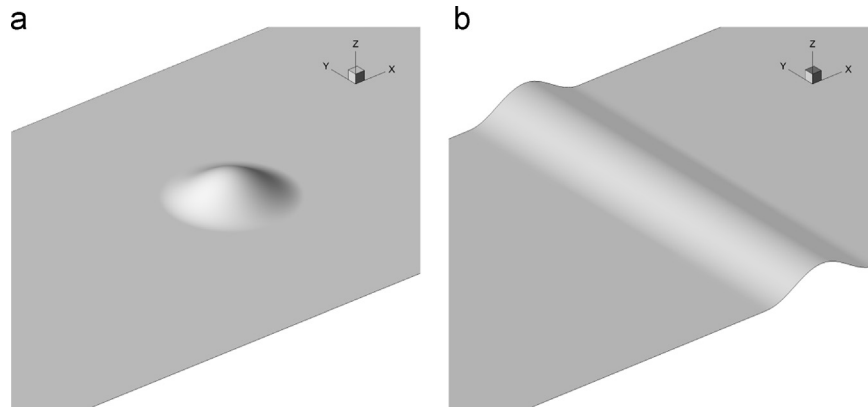


Fig. 4. Three dimensional views of (a) 3-D hill and (b) 2-D ridge.

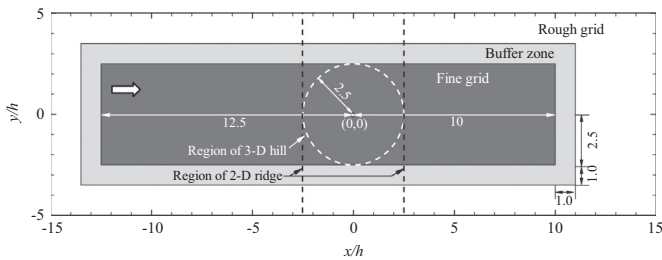


Fig. 5. Sketch map of the locations of the rough grid, buffer zone, and fine grid of the nested grid. White dashed line presents the region covered by a 3-D hill and black dashed line 2-D ridge.

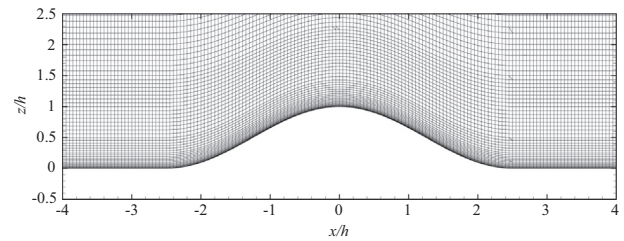


Fig. 6. Distributions of the mesh on the vertical slice crossing the center of the 3-D hill or the 2-D ridge.

blocks in detail. Mason and Thomson (1987) recommended a width of approximately 2 times the boundary layer depth as for reproducing the largest eddies in atmospheric boundary layer. As a result, with consideration of the convenience generating the roughness blocks, 1.8 times of the boundary layer thickness, 0.66 m, is determined. The upstream buffer zone, 2.0 m long, was appended to avoid any perturbations from the inlet condition into the turbulence generation region. The outlet of the numerical wind tunnel was set at the location with a distance of 2.4 m from the origin point, which is 60 times as large as the height of the simulated 3-D hill and 2-D ridge to avoid any influence from the outlet into the region of concern.

Same as the experimental study by Ishihara and Hibi (1998), 3-D hill has the shape $z_s(x, y) = h \cos^2 \pi(x^2 + y^2)^{1/2} / 2L$ and the 2-D ridge has the shape $z_s(x) = h \cos^2 \pi x / 2L$, where $h = 40$ mm and $L = 100$ mm. The maximum slope was thus about 32° . Fig. 3 shows the side view of the 3-D hill and 2-D ridge together with the coordinate system used in the study, where x , y and z are the streamwise, spanwise and vertical directions, respectively. In the x -coordinate, zero is the center of the 3-D hill and 2-D ridge. A second vertical coordinate, $z' = z - z_s(x, y)$, is also used to denote the height above the local surface. Three dimensional views of the 3-D hill and 2-D ridge are shown in Fig. 4.

2.4. Mesh system

In this study vertical grid distribution does not change in the whole domain for the flat terrain, however, with the intent to quantitatively investigate the turbulent features near the target region, two nested grids were used as presented in Fig. 5 where the area colored by dark gray shows the fine grid region. The fine grid domain extends over $(L_x, L_y, L_z) = (22.5h, 5h, 22.5h)$ in the x (streamwise), y (spanwise) and z (vertical) directions. The length of

the upstream fine grid region, $12.5h$, is larger than that of the downstream one, $10h$, in order to provide enough upstream space to prevent the influence from the change of the grid size to be transported into the region near the region of concern. By changing the length of the upstream and downstream fine grid region, $12.5h$ upstream and $10h$ downstream has been found as the optimized ones. As could be found from the following discussion about the fluid visualizations, these two lengths are large enough to absorb the perturbations from the change of the grid at the beginning and the end of the fine grid domain. In the fine grid region, the horizontal grid shape is square. The horizontal resolution of 10 mm, 8 mm, 4 mm, 2 mm, 1.0 mm have been examined. At last the meshes with horizontal resolution of 2 mm and 1.0 mm show almost the same results, indicating that horizontal grid size of 1.0 mm gives grid independent results. Therefore, in the fine grid region horizontal grid size of 1.0 mm is used. In between the rough grid region, as shown by the white color, and the fine grid region, as shown by the dark gray color, a buffer zone, as shown by the light gray color in Fig. 5, the horizontal grid size increases from 1.0 mm, from the fine grid region, to 10 mm, connecting the rough grid region, is used. Horizontal grid shape in the buffer zone is triangle and has a growing factor of 1.2. In the rough grid region, the horizontal grid shape is square and uniform grid size of 10 mm is applied. This grid nesting procedure used here allows us to limit the impact of the symmetry conditions at the sides and to simulate the flow with an acceptable computational time. The cost would be much higher if only the finest resolution is used. The choice of the size and resolution of our nested domains results from a compromise between constraints related to the available computational time and the factor that the domain should be large enough to represent the largest eddies and fine enough to represent the smallest eddies of interest. In Fig. 5 white dashed line shows the area covered by the 3-D hill and the black dashed lines show that by 2-D ridge. In the vertical direction, the vertical grid size of the first grid is $0.005h$ and the maximum growing ratio is 1.15. $y +$

on the surface of the target region is in between 0.5 and 1.0. The total grid number is 27.4million. When 3-D hill or 2-D ridge is set in the numerical wind tunnel, σ grid is applied to modify the locations of the vertical grid nodes. Fig. 6 shows the vertical slice crossing the origin point of the 3-D hill to provide one example how the σ grid works. Compared with the grid distribution of the mesh in flat terrain case, we can find that even the locations of the grid node are changed, the ratios of the vertical sizes of adjacent grids are kept as constants.

2.5. Boundary conditions of the numerical wind tunnel

As for boundary conditions, a stress-free condition was used at the top of the domain and a symmetry condition at the spanwise sides. Uniform wind flow with a constant speed of 5.4 m/s in time was set at the inlet. At the end of the wind tunnel, outlet boundary condition is applied, where the normal gradient of pressure and velocities are 0. Non-slip condition was used at the bottom surface where wall functions are applied.

2.6. Solution scheme and solution procedure

The 3D unsteady LES filtered Navier–Stokes equations are solved with the commercial CFD code ANSYS/Fluent6.3 (Fluent Inc., 2006) using the control volume method. The second-order central difference scheme is used for the convective and viscous terms, and the second-order implicit scheme is employed for the unsteady term. The SIMPLE (semi-implicit pressure linked

equations) algorithm is used to solve the discretized equations, which was shown by Ferziger and Peric (2002). Time step size is 0.0001 s.

After 2 s the initial transient effects were found to disappear, in another words the flow reached a stable stage. The turbulent fields were averaged in time over 6×10^4 instantaneous samples, collected every time step during a 6s period. A stable condition for time sampling can be achieved by evaluating relative errors in the mean streamwise velocity at $(x=0, y=0, z'=0.5h)$, which becomes less than 1% for the flat terrain, 3-D hill and 2-D ridge cases when the data from 2 s to 8 s are used. The time sampling error is calculated by finding the difference of the mean streamwise velocity at $(x=0, y=0, z'=0.5h)$ from 2 s to $2\text{ s}+T/2$ and that from $2\text{ s}+T/2$ to $2\text{ s}+T$, where T is the time used for time sampling.

3. Flow patterns

In the present study, with consideration of the computation stability, we chose 1×10^4 as the value for $C_f \gamma_0 / l_0$ in each grid occupied by the solid blocks. In the following validation, it can be found 1×10^4 for $C_f \gamma_0 / l_0$ is large enough and can reproduce the drag effects from the solid blocks very well.

It is interesting to look at the instantaneous flow fields across the nested grids. To show the different patterns of the flow over the flat terrain, 3-D hill and 2-D ridge, vorticities in z direction, $\partial v / \partial x - \partial u / \partial y$, at the slice of $z=1.0h$ at a given time $t=8\text{ s}$, are plotted in Fig. 7. As expected, turbulent structures appear much more detailed in the fine domain than in the coarse domain. The black dashed rectangle shows

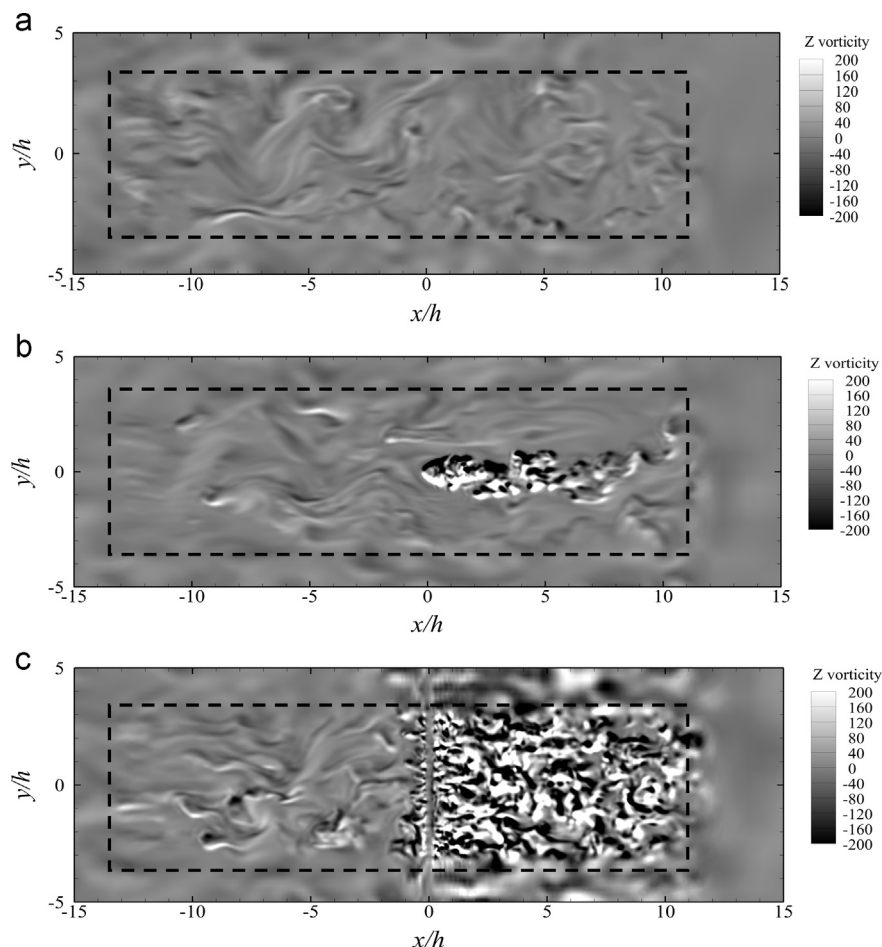


Fig. 7. Turbulence features of the flow, (a) over flat terrain, (b) in the wake of a 3-D hill and (c) in the wake of a 2-D ridge, at the height of h , visualized by the vorticity of vertical component.

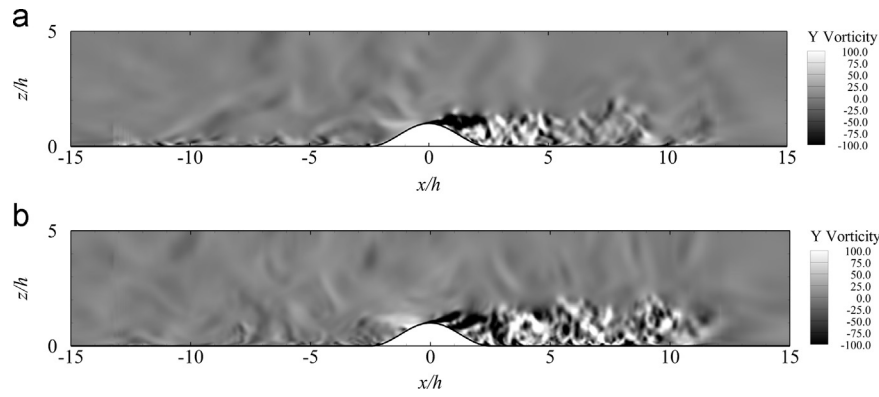


Fig. 8. Turbulence features of the flow in the wake of (a) 3-D hill and (b) 2-D ridge, on the vertical slice crossing $y=0$, visualized the vorticity of spanwise component.

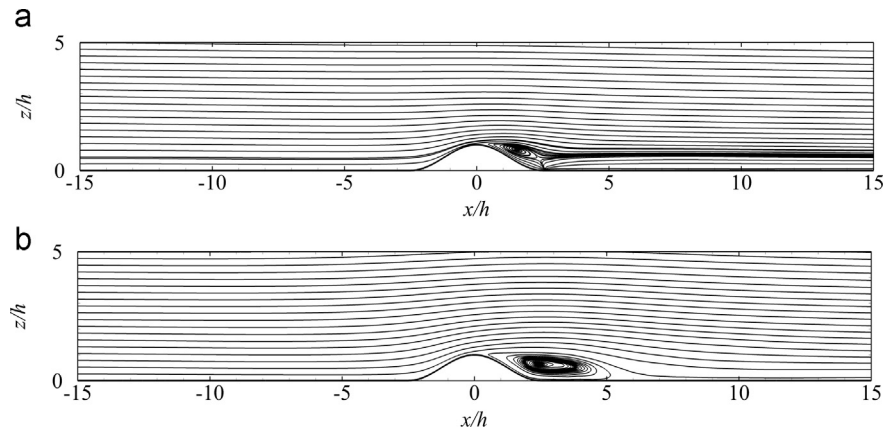


Fig. 9. Streamlines of the time averaged flow on the vertical slice crossing $y=0$, (a) 3-D hill and (b) 2-D ridge.

the region of fine and buffer grids. Some damping effects are visible at the inflow boundary of the fine grid domain. At the location of $x=0.0h$ the flow becomes stable and the perturbations from inlet of the fine grid domain becomes weak enough. It could also be found the influence from the outlet of the fine grid domain into the region of concern has been avoided. It means the fine grid space with length of $10h$ after the origin point is large enough. When we put a 3-D hill on the bottom of the numerical wind tunnel, the flow pattern in downstream regions shows quite different characteristics compared with that in the upstream region. The effects of the 3-D hill on the instantaneous wind generate a series of vortices clearly behind the summit. At this place the contrast between white and black areas becomes larger compared with that upstream of the hill, indicating a more intense turbulence in the wake. When a 2-D ridge is put on the bottom of the numerical wind tunnel, due to the disturbance of the ridge, some vortices with small size appear after the ridge, as shown in Fig. 7(c). The flow in the wake of 2-D ridge shows two dimensional features, i.e., the flow patterns do not change in the spanwise direction.

Fig. 8 shows the predicted instantaneous contour of the vorticity of y component $\partial w/\partial x - \partial u/\partial z$ in the slice of $y=0$ for the 3-D hill and 2-D ridge. The flow patterns for both cases are considerable different in the wake region. The flow in the wake of 3-D hill and 2-D ridge contains many small vortices with high intensity, but when the fluid flow downstream the turbulence strength for the 3-D hill becomes weak much more quickly than that for 2-D ridge.

Mean velocity streamlines in the representative cross-section, $y=0$, are depicted in Fig. 9. In the wake of 3-D hill, due to the existence of the mean spanwise flow, the streamlines are opened, as has been discussed by Ishihara and Hibi (2002) in detail from the view of continuity governing equation, and the flow recovers much more quickly in the wake of 3-D hill than that in the wake of 2-D ridge.

4. Turbulent statistics

4.1. Flat terrain

The flow over hills is very sensitive to the turbulence of the oncoming ABL, therefore it is meaningful to firstly examine if the oncoming ABL has been reproduced well. Fig. 10(a) shows the comparison of mean velocity profiles between the present simulation and the experiments by Ishihara et al. (1999). The vertical coordinate is normalized by h and the mean velocities are normalized by U_{ref} , which is the mean velocity at the height of $4h$ when the terrain is flat, 5.2 m/s. Good agreement is achieved. Turbulent boundary layer depth, δ , in both experiment and simulation is 360 mm, or 9.0 times of the height of 3-D hill and 2-D ridge.

The generated inflow turbulence statistics are in satisfactory agreement with the experimental data as could be found in Fig. 10(b). It is seen that the maximum value of σ_u , occurring close to the bottom of the wind tunnel, in simulation is considerably larger than experiments, which could also be found in the previous LES simulations, e.g. Tamura et al. (2007), Iizuka and Kondo (2004). The reason of this overestimation properly comes from the difference of the conditions on the bottom in experiments and simulations. In the simulation, the bottom of the numerical wind tunnel is absolutely smooth; however, in the experiment the bottom could not be smooth absolutely, which will disturb the flow near the bottom. The spanwise and vertical component of turbulence in the simulation fits experiments very well. The vertical profiles of mean velocities as well as three components of fluctuations at the locations of $x=-L, y=0$ and $x=L, y=0$ are also extracted and compared with those at $x=0, y=0$. The comparisons between them are in good agreement (not shown in the figure), implying a fully developed and stable boundary layer.

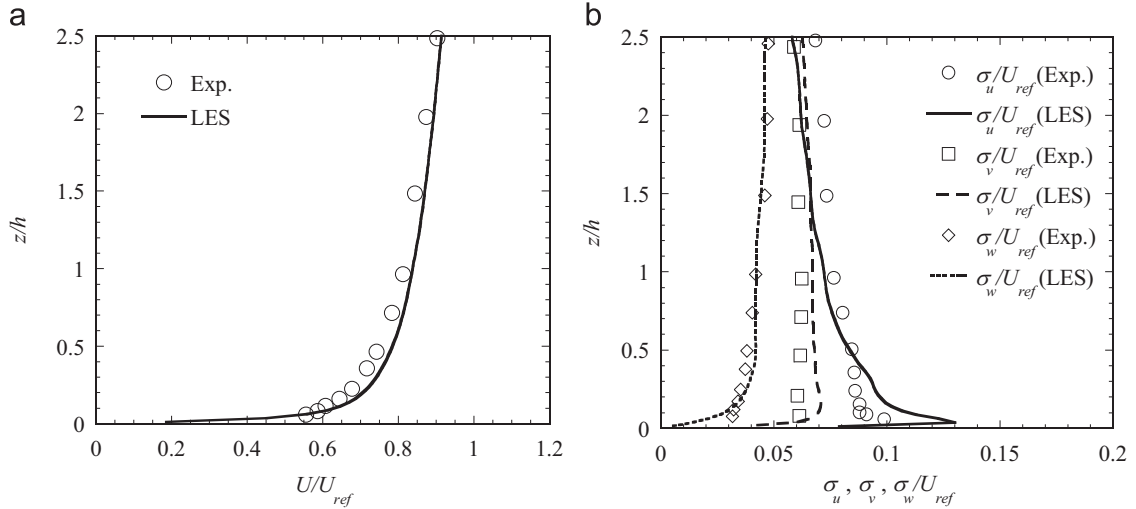


Fig. 10. Vertical profiles of (a) normalized mean velocity and (b) normalized turbulence fluctuations of the flow over flat terrain at the site of $x=0, y=0$.

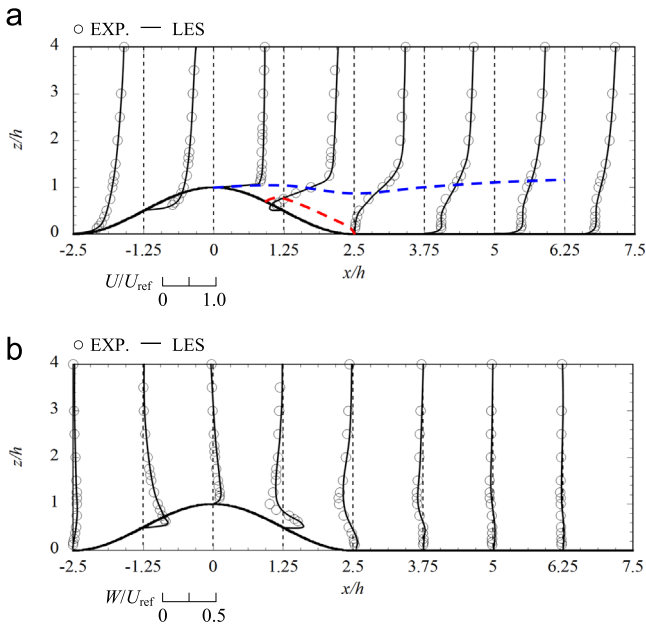


Fig. 11. Profiles of the normalized mean velocities of the flow over 3-D hill, (a) streamwise component and (b) vertical component on the vertical slice crossing $y=0$. (For interpretation of the references to color in this figure legend, the reader is referred to the web version of this article.)

4.2. 3-D hill

4.2.1. Profiles of mean velocities

Vertical profiles of streamwise and vertical mean velocities at several locations from $x=-2.5h$ to $x=6.25h$ with a step size of $1.25h$ for the 3-D hill are shown in Fig. 11(a) and Fig. 11(b) respectively. The profiles are normalized by U_{ref} . On the whole, the numerical results provide acceptable agreement with those in experiment for the mean velocity components.

At the upwind side, the streamwise mean velocity shows an obvious acceleration at the crest of the hill where the vertical gradient of the streamwise mean velocity versus the height shows high value, see Fig. 11(a). After the crest, the flow separation could be clearly identified. The reverse point, at which the flow direction is changed from positive to negative as approaching the surface, emerges. The height of the reverse point decreases as increase the downstream distance and attaches the ground at the foot of the

hill. By connecting the reverse points, as shown by the red dashed line superimposed on Fig. 11(a), the region of the separation bubble could be identified which starts at $x=0.9h$ and ends at $x=2.5h$, same with the results from experiments by Ishihara et al. (2001). The blue dashed line is the connection of points where the maximum vertical gradient of the mean streamwise velocity occurs. It is also the location of the separate shear layer where the fluctuations of the streamwise component show peak values as could be found in Fig. 12(a).

The magnitude of the mean vertical velocity component is much smaller than that of streamwise component, as a result, in order to clearly show the comparison between the simulation and experiment, the scale of the plotting for the mean vertical velocity is half of that for the streamwise component. It can be found from Fig. 11(b) that the vertical velocity is not as sensitive as the streamwise component to the disturbance of the 3-D hill. After $x=5h$, the vertical velocity shows almost zero profiles which means the vertical profiles have recovered to its origin state hereafter.

4.2.2. Profiles of fluctuations

It is now interesting to consider the evolution of turbulence, therefore the vertical profiles of normalized fluctuations by U_{ref} are plotted as shown in Fig. 12, where Fig. 12(a) is for the streamwise component, σ_u , Fig. 12(b) is for the spanwise component, σ_v , and Fig. 12(c) is for the vertical component, σ_w . At the foot of upwind side of the 3-D hill, the profiles of turbulent fluctuations give good agreement between the numerical prediction and the experimental data. At the lee side of the hill the simulated results are comparable with the experimental data as a whole, however, for the spanwise component, σ_v , and the vertical component, σ_w , in the range from $x=2.5h$ to $x=3.75h$, the LES results slightly overestimate the experiment. A very sharp peak occurs at the crest for σ_u , which is also observed in the simulations by Tamura et al. (2007) and Cao et al. (2012). The reason of the difference perhaps emerges from the different wall conditions between the numerical model and the real experimental model as well. The locations of the separated shear layer where the peaks of σ_u are very well reproduced and the shapes of the profiles are almost same. Another interesting behavior in the wake of the 3-D hill is that σ_v profiles show second local maximum in the wall layer. Ishihara et al. (1999) has pointed out that these second local peaks result from a low frequency motion of the fluid in the wall layer behind the hill.

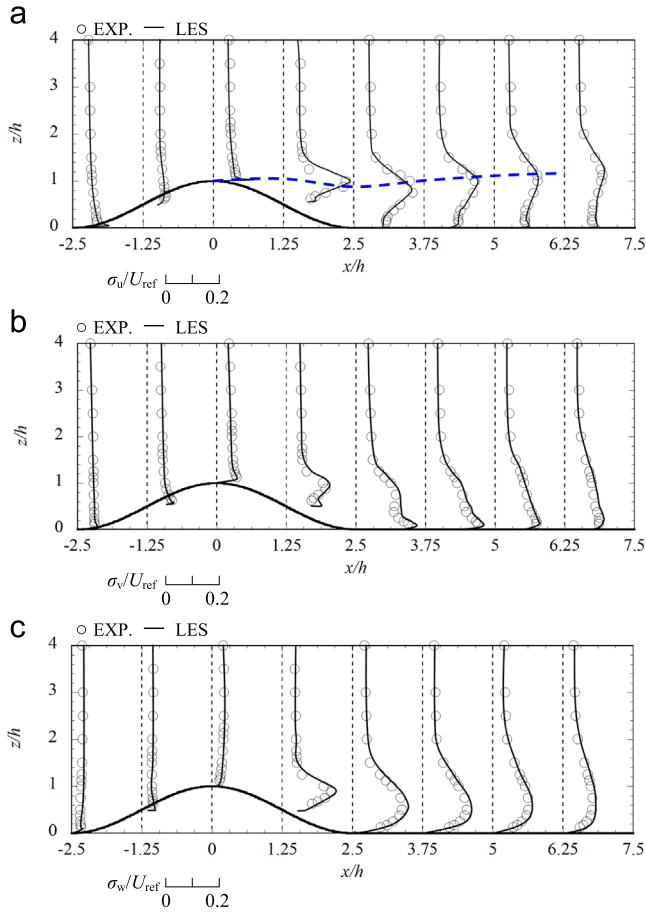


Fig. 12. Profiles of the normalized turbulence fluctuations of the flow over 3-D hill, (a) streamwise component, (b) spanwise component and (c) vertical component on the vertical slice crossing $y=0$.

4.3. 2-D ridge

4.3.1. Profiles of mean velocities

Profiles of mean velocity components for the 2-D ridge, as shown in Fig. 13, are normalized and scaled in the same way as those of the 3-D hill for a clearly comparison between them. The shear layer and the region of separation bubble are determined and drawn as the above presentations. Except some little discrepancies in the wake region, the prediction of mean velocities overall provides good agreement with the experimental data. The profiles of mean streamwise velocity in the far wake region show that the recovery of the wind speed becomes slower when the ground topography is 2-D ridge compared with 3-D hill and separation bubble becomes larger. The separation point and reattachment point locate at $1.2h$ and $4.7h$ respectively. The locations of separation point and reattachment point are close to the experimental results by Ishihara et al. (2001).

4.3.2. Profiles of fluctuations

The vertical profiles of normalized normal Reynolds stresses in the wake of the 2-D ridge shows different characteristics with those of the 3-D hill, see Fig. 14. The height under which the profiles are distorted in the case of 2-D hill is much higher than 3-D hill. Satisfactory agreements with the experiments are achieved. The magnitude of σ_u in the far wake region of 2-D ridge, see Fig. 14(a), is larger compared with the case of 3-D hill, which is due to the factor that in the case of 3-D hill the flow with lower turbulence density around the wake could be transported into the wake region because of the existence of the mean spanwise flow in the wake (even it is zero at the central

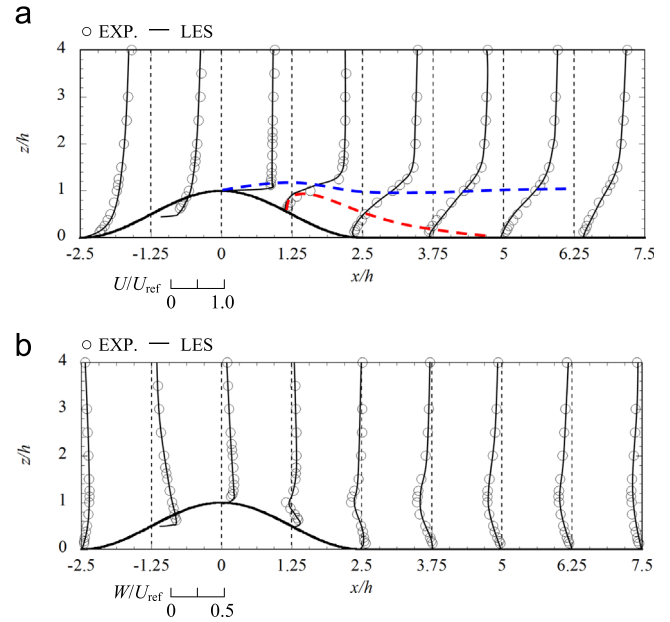


Fig. 13. Profiles of the normalized mean velocities of the flow over 2-D ridge, (a) streamwise component and (b) vertical component on the vertical slice crossing $y=0$.

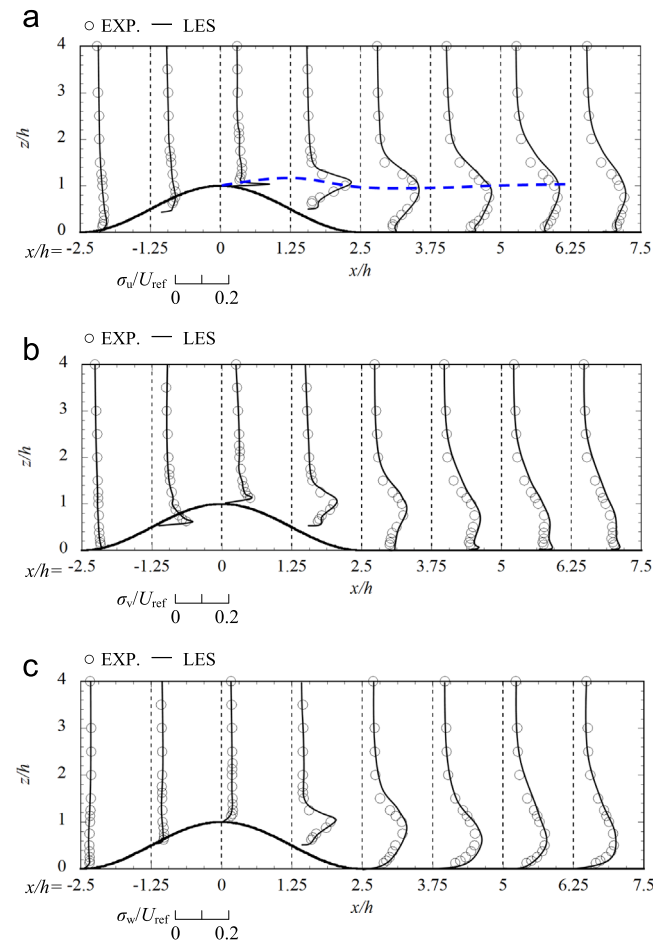


Fig. 14. Profiles of the normalized turbulence fluctuations of the flow over 2-D ridge, (a) streamwise component, (b) spanwise component and (c) vertical component on the vertical slice crossing $y=0$.

slice) and this low turbulence flow will mix with flow in the wake, as a result the turbulence in the wake of 3-D hill is reduced. In the case of 2-D ridge, the statistical flow field is not three dimensional but two

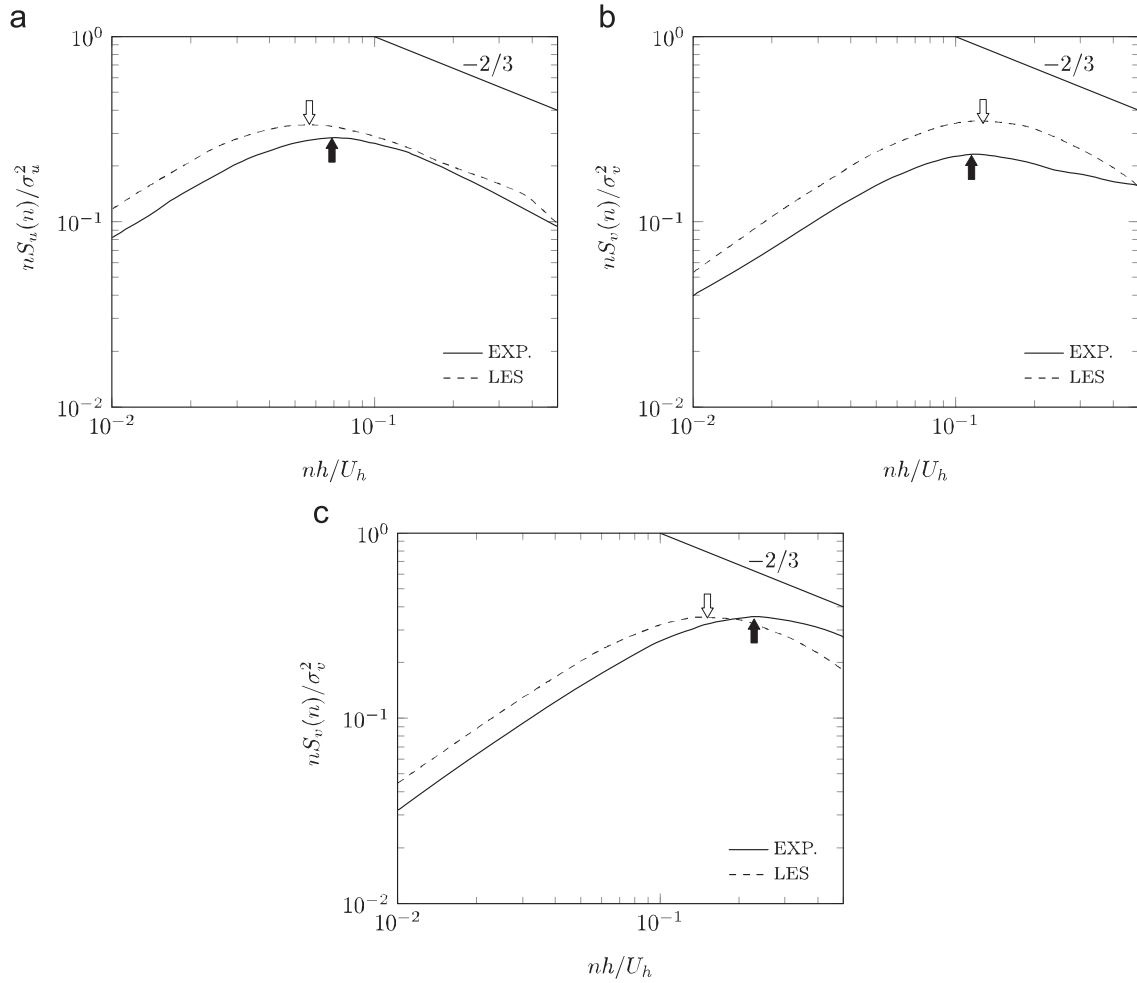


Fig. 15. Normalized power spectrum of velocity components for the flow over flat terrain at the site of $x=0, y=0, z=h$, (a) streamwise component, (b) spanwise component, (c) vertical component.

dimensional, i.e., the vertical distributions of the turbulence statistics does not change with the spanwise locations, therefore the mixing of flow in the spanwise direction could not occur. Some overestimations could be found for the fluctuations which were also found in the study by Cao et al. (2012) who applied LES turbulence model as well, therefore further research is deserved to be carried out in the future to understand the reasons of these discrepancies.

5. Power spectrum

With an attempt to analyze the dynamics of the eddy motions, we recorded the time histories of the velocities at several locations and the spectrum analysis was carried out. Maximum-entropy method (MEM) is used to obtain the smoothed spectra and the values are normalized by the standard deviations of fluctuating velocities. The spectrum are normalized against a non-dimensional frequency $f=nh/U_{ref}$, where n is the natural frequency in Hz.

5.1. Flat terrain

In order to verify the oncoming ABL flow and provide reference data for the following discussion about the dynamics of the eddy motions in the near-wake region of the 3-D hill and 2-D ridge, we investigate the power spectra of streamwise, u , spanwise, v , and vertical, w , velocities, as shown in Fig. 15. From the plots of simulation, it can be found that the normalized power spectra at $x=0$,

$y=0, z=h$ display a $-2/3$ slope in the inertial subrange, as predicted by Kolmogorov's hypothesis. Superimposed solid lines on Fig. 15 are the data from the experiment by Ishihara et al. (1999), which show overall good comparison with those from the present simulations. For the streamwise and vertical components, the simulated ones shift slightly toward the low frequency range, with the opposite being true for the spanwise component. This good agreement about the power spectrum is the indication that not only the turbulence statistics but also the dynamics of eddy motions are well reproduced for the oncoming flow. The hollow and solid arrows show the peaks of power spectrum in simulations and experiments respectively.

5.2. 3-D hill

At $x=3.75h, y=0, z=h$, the spectra of velocities for 3-D hill are plotted in Fig. 16 and show good comparison with those in experiments. The peaks at the spectra of v and w in simulation are 0.12 and 0.13 respectively which are very comparable with those of the flat terrain at the same height, however, the peak for the u spectrum shifts to the high frequency range, $nh/U_h=0.105$. In order to examine if the eddy structures in the wake of the topographies are sensitive to the oncoming flow conditions, roughness blocks were removed and the simulations were ran again. It is found that when the oncoming flow is laminar, the spectra of the velocities in the wake of 3-D hill do not show large deviations from the data when the oncoming flow is

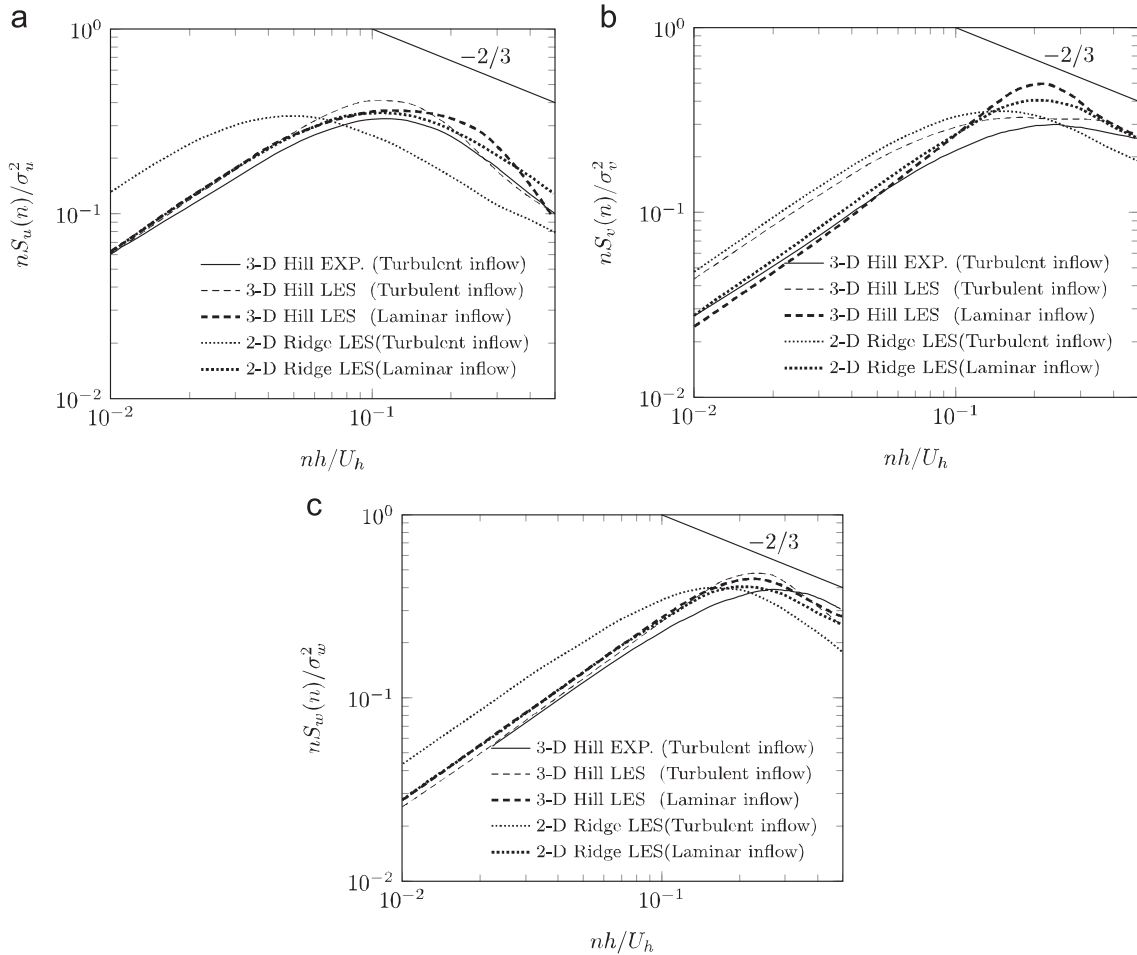


Fig. 16. Normalized power spectrum of velocity components for the flow over 3-D hill and 2-D ridge at the site of $x=3.75h$, $y=0$, $z=h$, (a) streamwise component, (b) spanwise component, (c) vertical component.

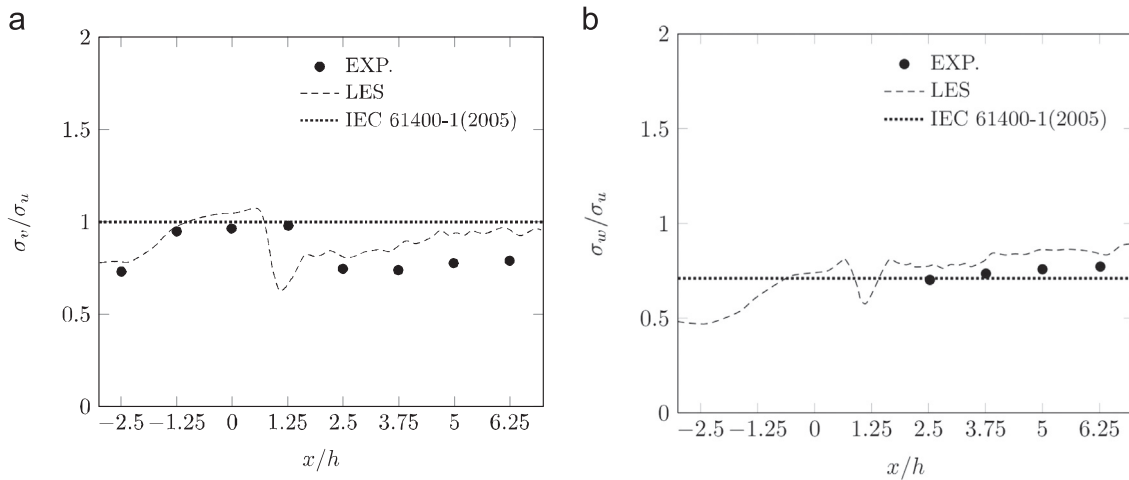


Fig. 17. Ratios of turbulence fluctuation on the line crossing the center of 3-D hill, $x=0$, $y=0$, with height of h relative to the surface. (a) σ_v/σ_u and (b) σ_w/σ_u .

turbulent, indicating that the eddy structures in the wake of 3-D hill are not sensitive to the oncoming flow conditions.

5.3. 2-D ridge

Unlike 3-D hill, the shapes of the u spectra of the 2-D hill at $x=3.75h$, $y=0$, $z=h$ roughly coincide with those of the oncoming

turbulent flow, see Fig. 16, indicating a similar turbulent structure between them. However, when the oncoming flow is laminar, in another word the topography is the sole source of turbulence in the wake, the peak of u spectrum shows a shift to high frequency range and presents a similar shape with that of 3-D hill. This result indicates that for the 2-D ridge when the oncoming flow is turbulent it will make the turbulence structure in the wake to be close to that of the flow

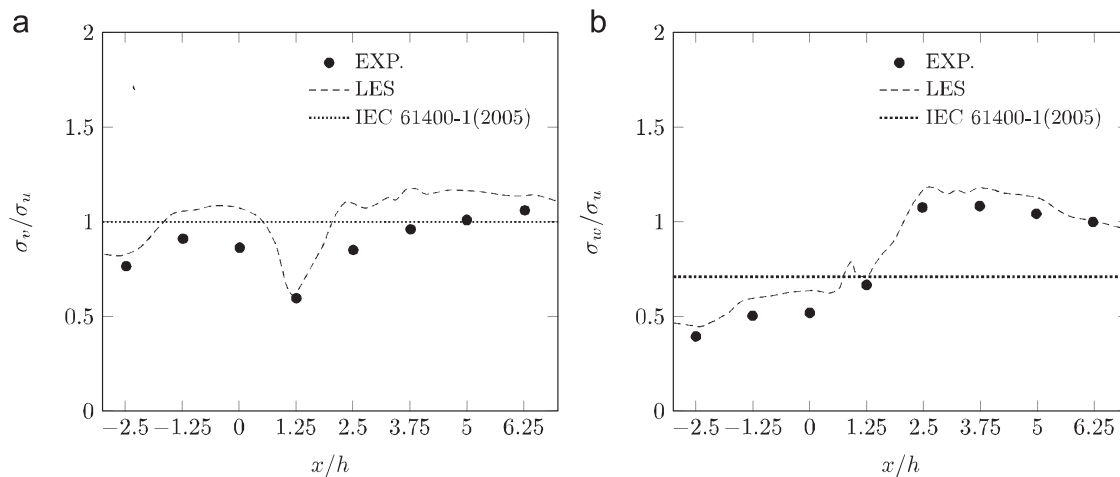


Fig. 18. Ratios of turbulence fluctuation on the line crossing the center of 2-D ridge, $x=0$, $y=0$, with height of h relative to the surface. (a) σ_v/σ_u and (b) σ_w/σ_u .

upstream, which is not the case for the 3-D hill. Therefore, we can conclude that for different kinds of terrain and different oncoming flow conditions the spectrum of the fluctuating velocities should be different.

6. Reynolds stress ratios

According to the standard IEC 61400-1 (2005), $\sigma_v/\sigma_u=0.7$ and $\sigma_w/\sigma_u=0.5$ are recommended when the terrain is flat. In the present simulation of flat terrain at the site of $x=0$, $y=0$, $z=h$, σ_v/σ_u and σ_w/σ_u are predicted as 0.81 and 0.49 respectively which are close to the data in IEC 61400-1 (2005).

In case of a wind turbine site is located within a complex terrain, IEC 61400-1 (2005) permits to increase the representative value by a factor C_{CT} defined as:

$$C_{CT} = \frac{\sqrt{1 + (\sigma_v/\sigma_u)^2 + (\sigma_w/\sigma_u)^2}}{1.375} \quad (9)$$

C_{CT} is intended to account for the distortion of turbulence structure by complex terrain and to be estimated based on site specific data at the turbine hub height. In the absence of site specific data, IEC 61400-1 (2005) recommends to use a correction factor of 1.15 or results of simulation. When $C_{CT} = 1.15$ and if the fluctuation ratios σ_v/σ_u and σ_w/σ_u are modified at the same rate, λ , this rate could be solved as 1.42. As a result, for the complex terrain, the upper limit of σ_v/σ_u and σ_w/σ_u becomes 1.0 and 0.71 respectively.

Numerically simulated and experimentally measured σ_v/σ_u and σ_w/σ_u at $z'=h$ for both 3-D hill and 2-D ridge are plotted in Fig. 17. The comparison between them are good. The recommended Reynolds stress ratios for the complex terrain in IEC 61400-1 (2005) are superimposed as well. It is found that, for both the simulation and the experiment, σ_v/σ_u and σ_w/σ_u proposed in IEC 61400-1 (2005) are appropriate for the case of 3-D hill and σ_v/σ_u for the case of 2-D ridge. However, the most striking thing is for σ_w/σ_u whose value gives very large increase in the near wake of 2-D ridge showing non-isotropic characteristics of turbulence. Therefore in the near wake of 2-D ridge the simulation or experimental results should be applied, which supports the concept modifying the ambient turbulence values for use in the wake of isolated hills in IEC 61400-1 (2005) (Fig. 18).

7. Conclusions

In this study the turbulent flow fields over a 3-D hill and a 2-D ridge with smooth ground are numerically predicted by large eddy

simulations. The mean velocity distributions, turbulent fluctuations, the spectra and the fluctuations ratios are examined. Following summarizes the conclusions in the present study.

1. A method simulating the roughness blocks by adding a drag force term in the momentum equation is applied. Through the method, it is not necessary to explicitly build the geometry of the blocks. The volumes occupied by the roughness blocks could be determined by some functions. Satisfactory results of the turbulent flow over flat terrain in simulation indicate that this method is accurate enough to simulate the roughness blocks.
2. Mean flow fields in both 3-D hill and 2-D ridge cases are well predicted by large eddy simulation. The separation point and the reattachment point in simulation agree well with those measured in experiments. Normalized turbulent fluctuations in simulations show fairly good agreement with experiments.
3. Spectra of the velocities in the wake of the 3-D hill, 2-D ridge and those over flat terrain are very comparable with those in experiments. The spectra of the velocities in the wake of the 2-D ridge shows the same trend with those of flat terrain, which is different for the 3-D hill. Another interesting finding is that the spectra of the flow in the wake of 3-D hill are not sensitive to the turbulence condition of the oncoming flow, but 2-D ridge is.
4. σ_w/σ_u gives very large increase in the near wake of 2-D ridge showing non-isotropic characteristics of turbulence. Therefore in the near wake of 2-D ridge the simulation or experimental results should be applied for the design of wind turbine, which supports the concept modifying the ambient turbulence values for use in the wake of isolated hills in IEC 61400-1 (2005).

Acknowledgments

Supports from the Project of Innovation-driven Plan in Central South University (2015CX006) and the National Natural Science Foundation of China (51322808 and U1534206) are gratefully acknowledged.

References

- Abdi, S., Bitsuamlak, G., 2014. Wind flow simulations on idealized and real complex terrain using various turbulence models. *Adv. Eng. Softw.* 75, 30–41.
- Bitsuamlak, G., Stathopoulos, T., Bédard, C., 2004. Numerical evaluation of wind flow over complex terrain: review. *J. Aerosp. Eng.* 17, 135–145.
- Bitsuamlak, G., Stathopoulos, T., Bédard, C., 2004. Numerical modeling of wind flow over different types of topography. *Structures*, 1–11.

- Blocken, B., Hout, A., Dekker, J., Weiler, O., 2015. CFD simulation of wind flow over natural complex terrain: case study with validation by field measurements for Ria de Ferrol, Galicia, Spain. *J. Wind. Eng. Ind. Aerodyn.* 147, 43–57.
- Cao, S., Tamura, T., 2006. Experimental study on roughness effects on turbulent boundary layer flow over a two-dimensional steep hill. *J. Wind. Eng. Ind. Aerodyn.* 94, 1–19.
- Cao, S., Wang, T., Ge, Y., Tamura, Y., 2012. Numerical study on turbulent boundary layers over two-dimensional hills – effects of surface roughness and slope. *J. Wind. Eng. Ind. Aerodyn.* 104–106, 342–349.
- Diebold, M., Higgins, C., Fang, J., Bechmann, A., Parlange, M.B., 2013. Flow over hills: a large-eddy simulation of the bolund case. *Bound. Layer. Meteorol.* 148, 177–194.
- Ferreira, A.D., Lopes, A.M.G., Viegas, D.X., Sousa, A.C.M., 1995. Experimental and numerical simulation of flow around two-dimensional hills. *J. Wind. Eng. Ind. Aerodyn.* 54–55, 173–181.
- Ferziger, J., Peric, M., 2002. *Computational Method for Fluid Dynamics*, third ed. Springer, Berlin.
- Fluent Inc, 2006. *Fluent 6.3 User's Guide*. Fluent Inc, Lebanon.
- Gong, W., Ibbetson, A., 1989. A wind tunnel study of turbulent flow over model hills. *Bound. Layer. Meteorol.* 49, 113–148.
- IEC 61400-1, 2005. *Wind turbines, Part 1, Design requirements*, 56.
- Iizuka, S., Kondo, H., 2004. Performance of various sub-grid scale models in large-eddy simulations of turbulent flow over complex terrain. *Atmos. Environ.* 38, 7083–7091.
- Iizuka, S., Kondo, H., 2006. Large-eddy simulations of turbulent flow over complex terrain using modified static eddy viscosity models. *Atmos. Environ.* 40, 925–935.
- Ishihara, T., Hibi, K., 2002. Numerical study of turbulent wake flow behind a three-dimensional steep hill. *Wind. Struct.* 5, 317–328.
- Ishihara, T., Hibi, K., Oikawa, S., 1999. A wind tunnel study of turbulent flow over a three-dimensional steep hill. *J. Wind. Eng. Ind. Aerodyn.* 83, 95–107.
- Ishihara, T., Fujino, Y., Hibi, K., 2001. A wind tunnel study of separated flow over a two-dimensional ridge and a circular hill. *J. Wind. Eng.* 89, 573–576.
- Ishihara, T., Hibi, K., 1998. An experimental study of turbulent boundary layer over steep hills. In: *Proceedings of the 15th Japan National Symposium on Wind Engineering*. 61–66.
- Kaimal, J.C., Finnigan, J.J., 1994. *Atmospheric Boundary Layer Flows*. Oxford University Press, Oxford.
- Lun, Y.F., Mochida, A., Murakami, S., Yoshino, H., Shirasawa, T., 2003. Numerical simulation of flow over topographic features by revised $k-\epsilon$ models. *J. Wind. Eng. Ind. Aerodyn.* 91, 231–245.
- Mason, P.J., Thomson, D.J., 1987. Large-eddy simulations of the neutral-static-stability planetary boundary layer. *Q. J. R. Meteorol. Soc.* 113, 413–443.
- Sajjadi, S.G., Craft, T.J., Feng, Y., 2001. A numerical study of turbulent flow over a two-dimensional hill. *Int. J. Numer. Methods Fluids* 35, 1–23.
- Smagorinsky, J., 1963. General circulation experiments with the primitive equations. I. The basic experiment. *Mon. Weather Rev.* 91, 99–164.
- Tamura, T., Cao, S., Okuno, A., 2007. LES study of turbulent boundary layer over a smooth and a rough 2D hill model. *Flow Turbul. Combust.* 79, 257–266.
- Wan, F., Porté-Agel, F., 2011. Large-eddy simulation of stably-stratified flow over a steep hill. *Boundary-Layer Meteorol.* 138 (3), 367–384.
- Yamaguchi, A., Enoki, K., Ishihara, T., 2009. A generalized canopy model for the wind prediction in the forest and the urban area. *APCWE-VII*, Taiwan.